Angularly multiplexed spectral imager

Jonathan M. Mooney

Rome Laboratory
Hanscom AFB, MA 01731

ABSTRACT

A spectral imager constructs a three dimensional (two spatial and one spectral) image from a series of two dimensional images. This paper discusses a technique for spectral imaging that multiplexes the the spatial and spectral information on the focal plane, then demultiplexes the resulting imagery to obtain the spectral image. The resulting spectral image consists of 184 x 184 spatial pixels and 40 spectral bands. The current implementation operates over the 3-5μm band, but can easily be applied to other spectral regions. A hardware description, the mathematical development and experimental results are presented.

1. BACKGROUND

Most spectral imagers slice the three dimensional image into a sequence of two dimensional images. Two common approaches are: 1) image in the two spatial dimensions while using a sequence of spectral filters to slice in the spectral domain, or 2) image in one spatial and one spectral dimension while scanning a slit over the remaining spatial direction. Each of these approaches are inherently inefficient. In the first case only one color is imaged at a time. If N_λ spectral bands are to be imaged, then the efficiency is $(1/N_\lambda)$. In the second case only one slit of the scene is imaged at a time. If N_xxN_y spatial resolution elements are to be imaged by scanning in the x direction, then the efficiency will be $(1/N_x)$.

Color visible CCDs achieve spectral imaging by using dichroic filters such that each pixel detects either red, green or blue light. The efficiency of these devices is at best 1/3, and they also suffer from a degradation in spatial resolution by $1/\sqrt{3}$. This approach is limited to imaging no more than a few colors.

Though most spectral imaging techniques suffer from a degradation in efficiency, resolution or both; there are two noteworthy exceptions. One is to use a cascade of spectral beam splitters with a separate imaging focal plane for each color. The efficiency of this approach is determined by that of the beam splitters and in theory can be 100%; however, practical constraints limit application of this approach to resolution of no more than a few spectral bands. The other exception is Fourier transform spectroscopy. A Fourier transform spectrometer uses an interferometer to multiplex the spectral information. Both lateral shear and longitudinal displacement interferometers are used. Lateral shear interferometers use common path interferometers that multiplex the spatial and spectral information in space; they are relatively insensitive to vibration and often find application in field measurements. Longitudinal displacement interferometers multiplex the spectral information in time; they are susceptible to vibrations and usually find application in laboratories. A Fourier transform imaging spectrometer based on a lateral shear interferometer would have the same efficiency limit as a scanned slit spectrometer, while that based on a longitudinal displacement interferometer could have very high efficiency but would be useful only in low vibration environments.

Each of these imaging techniques is a example of tomographic imaging. In effect the object is imaged as a sequence of slices. In the field of medicine, tomographic imaging was greatly enhanced by the application of computers to the image reconstruction. Computers enabled medical researchers to obtain as large a signal to noise ratio as possible from as few photons as possible (x-rays). The spectral imaging problem is similar in that one would like the largest signal to noise ratio possible from the available photons. It is for this reason that we investigate the application of medical computer aided tomography techniques to spectral imaging.

0-8194-1833-1/95/$6.00

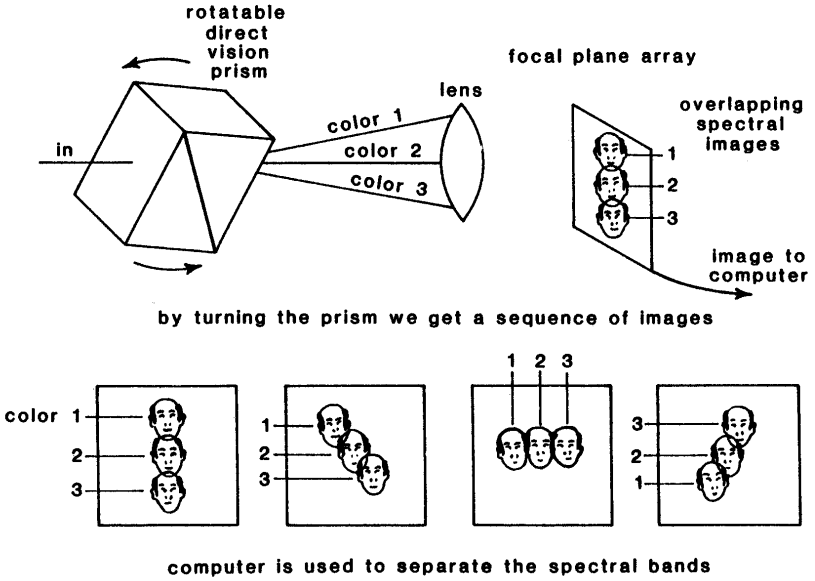

Figure 1: Schematic representation of the direct vision prism approach to the Angularly Multiplexed Spectral Imager (AMSI). By rotating the prism between exposures, one obtains a sequence of two-dimensional images that can be used to reconstruct the three-dimensional image.

Several recent papers have discussed application of computed tomography techniques to spectral imaging[1, 2, 3, 4]. In the angularly multiplexed spectral imager the spatial and spectral information are multiplexed via a rotating direct vision prism. This technique is unique in its high efficiency, and in the inversion algorithm used. The inversion algorithm is well suited to a large number of spectral imaging techniques[5].

2. HARDWARE CONFIGURATION

Figure 1 is a schematic representation of the data collection hardware of the Angularly Multiplexed Spectral Imager. It consists of an infrared camera and a direct vision prism. The direct vision prism disperses light, but leaves one wavelength undeviated. In this is work we wish to image over the 3-5μm band, so 4.0μm light passes through the prism undeviated. The imagery, as recorded by the infrared camera, is blurred in the dispersion direction. As the sequence of frames is recorded, the direct vision prism is rotated, and the image of each chromatic band follows a circular path with the radius of the path determined by the prism dispersion and objective focal length. Each of the recorded images contains a linear superposition of each spectral image convolved with a unique point spread function.

The infrared camera was fabricated in-house and consisted of a FLIR systems non-interlaced 320x244 PtSi focal plane array in a pour-filled liquid Nitrogen dewar. A 27mm focal-length lens was used to form the image on the focal plane. A real field stop was obtained using two 50mm lenses functioning as a 1:1 relay with the stop mid-way between the two lenses. The field stop limited the effective field of view to 184x184 pixels. The direct vision prism

was located between the last element of the relay and the 27mm lens. This combination of elements spread the 3-5μm band over 40 pixels.

The data acquisition was accomplished by continuously rotating the prism and storing the 12-bit data in a frame buffer. (The non-interlaced architecture of the FLIR systems focal plane array made continuous rotation possible.) A complete data set consisted of 80 consecutive frames at angular increments uniformly distributed over 2π. The frame buffer was built in-house, and was interfaced to a Sun workstation.

3. INTRODUCTION TO THE IMAGE CONSTRUCTION ALGORITHM

The development of the inversion algorithm is based on the observation that on the sequence of recorded images, the image of each chromatic band follows a circular path with the radius of the path determined by the prism dispersion. Each of the recorded images contains a linear superposition of each spectral image convolved with a unique point spread function.

For example, assume that we want to construct a three color image of some scene $c(x, y, \lambda)$. We divide the scene into three spectral bands, $c_1(x, y), c_2(x, y)$ and $c_3(x, y)$. The data that is recorded by the computer will be

$$\begin{aligned} r_1(x,y) &= p_{11}(x,y) ** c_1(x,y) + p_{12}(x,y) ** c_2(x,y) + p_{13}(x,y) ** c_3(x,y) \\ r_2(x,y) &= p_{21}(x,y) ** c_1(x,y) + p_{22}(x,y) ** c_2(x,y) + p_{23}(x,y) ** c_3(x,y) \\ r_3(x,y) &= p_{31}(x,y) ** c_1(x,y) + p_{32}(x,y) ** c_2(x,y) + p_{33}(x,y) ** c_3(x,y), \end{aligned} \tag{1}$$

where $r_a(x, y)$ is the data recorded for frame a at location (x, y), $p_{ab}(x, y)$ is the point spread function of spectral band b recorded on image a, and $**$ indicates a two dimensional convolution. Each of the $r_1(x, y), r_2(x, y)$ and $r_3(x, y)$ correspond to the recorded image for a different angular orientation of the direct vision prism.

We wish to solve the system of equations Eq. 1 for $c_b(x, y)$. First we take the spatial two dimensional Fourier transform of each equation.

$$\begin{aligned} R_1(\xi,\zeta) &= P_{11}(\xi,\zeta)C_1(\xi,\zeta) + P_{12}(\xi,\zeta)C_2(\xi,\zeta) + P_{13}(\xi,\zeta)C_3(\xi,\zeta) \\ R_2(\xi,\zeta) &= P_{21}(\xi,\zeta)C_1(\xi,\zeta) + P_{22}(\xi,\zeta)C_2(\xi,\zeta) + P_{23}(\xi,\zeta)C_3(\xi,\zeta) \\ R_3(\xi,\zeta) &= P_{31}(\xi,\zeta)C_1(\xi,\zeta) + P_{32}(\xi,\zeta)C_2(\xi,\zeta) + P_{33}(\xi,\zeta)C_3(\xi,\zeta), \end{aligned} \tag{2}$$

where we use capital letters to indicate that we have Fourier transformed, and ξ and ζ are the spatial frequency variables. The form of Eq. 2 can be reduced to

$$\begin{bmatrix} R_1(\xi,\zeta) \\ R_2(\xi,\zeta) \\ R_3(\xi,\zeta) \end{bmatrix} = \begin{bmatrix} P_{11}(\xi,\zeta) & P_{12}(\xi,\zeta) & P_{13}(\xi,\zeta) \\ P_{21}(\xi,\zeta) & P_{22}(\xi,\zeta) & P_{23}(\xi,\zeta) \\ P_{31}(\xi,\zeta) & P_{32}(\xi,\zeta) & P_{33}(\xi,\zeta) \end{bmatrix} \begin{bmatrix} C_1(\xi,\zeta) \\ C_2(\xi,\zeta) \\ C_3(\xi,\zeta) \end{bmatrix}, \tag{3}$$

which is simply a large array of vector-matrix multiplications

$$\vec{R}(\xi,\zeta) = \boldsymbol{P}(\xi,\zeta)\vec{C}(\xi,\zeta). \tag{4}$$

In order to reconstruct the an image of the object from the recorded data, we pre-multiply both sides of Eq. 4 by $\boldsymbol{P}^{-1}(\xi,\zeta)$

$$\vec{C}(\xi,\zeta) = \boldsymbol{P}^{-1}(\xi,\zeta)\vec{R}(\xi,\zeta). \tag{5}$$

The constructed spectral image is obtained by taking the inverse Fourier transform of $\vec{C}(\xi,\zeta)$.

From this development we can see that if the recorded data can be represented as a superposition of two-dimensional chromatic images (which is often the case for spectral imaging), then the inversion technique developed here can be used to construct a three-dimensional image.

4. A MORE FORMAL MATHEMATICAL DEVELOPMENT

The previous section should be thought of as a road map to this section. This section will be more specific about assumptions, and arrive at an expression for the matrix $\boldsymbol{P}(\xi,\zeta)$, but is essentially a second trip through the same landscape.

Assume that we image a scene through a direct vision prism with a staring sensor. The effective focal length of the sensor is f and the dispersion of the direct vision prism is given by the function $\theta(\lambda-\lambda_o)$ where $\theta(0)=0.0$. The image of the scene is given by $r(x,y,\phi)$, where x and y are the spatial coordinates and ϕ is the angular orientation of the prism with respect to the staring sensor. We find

$$r(x,y,\phi)=\int_{\lambda_1}^{\lambda_2}\int_{-\infty}^{\infty}\int_{-\infty}^{\infty} c(x'-f\cos(\phi)\tan(\theta(\lambda-\lambda_o)),y'-f\sin(\phi)\tan(\theta(\lambda-\lambda_o)),\lambda)$$
$$\text{rect}\left(\frac{x-x'}{\Delta x}\right)\text{rect}\left(\frac{y-y'}{\Delta y}\right)\eta(\lambda)dx'dy'd\lambda, \tag{6}$$

where $\eta(\lambda)$ is the quantum efficiency of the sensor as a function of wavelength (including the effects of filters and windows), λ_1 and λ_2 bound the spectral response of the sensor, the integration over x and y indicates convolution with the pixel active area, Δx and Δy are the pixel dimensions, and $c(x,y,\lambda)$ is the image at the focal plane.

In order to simplify this development, we will assume that $\tan(\theta(\lambda-\lambda_o))=\alpha(\lambda-\lambda_o)$, where α is a constant. We proceed by breaking the integration over wavelength into a sum of integrations over wavelength intervals. We define the center wavelength of each interval λ_n by $\alpha(\lambda_n-\lambda_o)=n\Delta z/f$, where n is an integer and Δz is a spatial dimension on the focal plane on the order of a pixel size. At this point we have

$$r(x,y,\phi)=\sum_{n=-N_\lambda/2}^{N_\lambda/2-1}\int_{-\infty}^{\infty}\int_{-\infty}^{\infty}\int_{-\infty}^{\infty} c(x'-f\alpha\cos(\phi)(\lambda-\lambda_o),y'-f\alpha\sin(\phi)(\lambda-\lambda_o),\lambda)$$
$$\text{rect}\left(\frac{x-x'}{\Delta x}\right)\text{rect}\left(\frac{y-y'}{\Delta y}\right)\text{rect}\left(\frac{\lambda_n-\lambda}{\Delta\lambda}\right)\eta(\lambda)dx'dy'd\lambda, \tag{7}$$

where N_λ is the number of color increments required to span the chromatic sensitivity of the imaging system and is given by $N_\lambda=f\alpha(\lambda_2-\lambda_1)/\Delta z$, and $\Delta\lambda=\Delta z/\alpha f$.

The next step is to take the Fourier transform of $r(x,y,\phi)$ over the spatial variables (i.e. x and y); however, this Fourier transform operation will be executed discretely on a computer, so we treat it as such

$$R(\xi,\zeta,\phi)=\frac{1}{N_xN_y}\sum_{j=0}^{N_x-1}\sum_{k=0}^{N_y-1}\sum_{n=-N_\lambda/2}^{N_\lambda/2-1}\int\int\int_{-\infty}^{\infty} c(x'-f\alpha\cos(\phi)(\lambda-\lambda_o),y'-f\alpha\sin(\phi)(\lambda-\lambda_o),\lambda)$$
$$\text{rect}\left(\frac{j\delta x-x'}{\Delta x}\right)\text{rect}\left(\frac{k\delta y-y'}{\Delta y}\right)\text{rect}\left(\frac{\lambda_n-\lambda}{\Delta\lambda}\right)e^{-2\pi i\xi j\delta x}e^{-2\pi i\zeta k\delta y}\eta(\lambda)dx'dy'd\lambda, \tag{8}$$

where we have explicitly indicated the effect of discrete sampling via indices j and k, and sampling intervals δx and δy.

Since $\delta x\geq\Delta x$, at most one of the terms in the sum over j and k will be non-zero. The non-zero terms will occur when $|j\delta x-x'|<\Delta x/2$ and when $|k\delta y-y'|<\Delta y/2$. The easiest way to proceed is to make the approximation that the non-zero terms occur when $j\delta x=x'$ and when $k\delta y=y'$. This is an excellent approximation at low spatial frequencies, but may cause problems at high spatial frequencies. We will proceed by making this approximation, but must keep in mind that scenes with a great deal of high spatial frequency energy may cause problems.

After a bit of manipulation we arrive at

$$R(\xi,\zeta,\phi) = \frac{1}{N_x N_y} \sum_{n=-N_\lambda/2}^{N_\lambda/2-1} \int_{\lambda_n-\Delta\lambda/2}^{\lambda_n+\Delta\lambda/2} C(\xi,\zeta,\lambda) e^{-2\pi i f(\xi\cos(\phi)+\zeta\sin(\phi))\alpha(\lambda-\lambda_o)} \eta(\lambda) d\lambda, \tag{9}$$

where $C(\xi,\zeta,\lambda)$ is the two dimensional discrete Fourier transform of $c(x,y,\lambda)$.

If we assume that $C(\xi,\zeta,\lambda)$ and $\eta(\lambda)$ are slowly varying functions of λ over the integration interval, we can bring them out of the integral. After further manipulation we find

$$R(\xi,\zeta,\phi) = \frac{\Delta z}{N_x N_y f\alpha} \mathrm{sinc}(\Delta z(\xi\cos(\phi)+\zeta\sin(\phi))) \sum_{n=-N_\lambda/2}^{N_\lambda/2-1} e^{-2\pi i(\xi\cos(\phi)+\zeta\sin(\phi))n\Delta z} C(\xi,\zeta,\lambda_n)\eta(\lambda_n). \tag{10}$$

This equation can easily be recast into matrix notation. Since the value of ϕ will take on discrete values ϕ_m, we get

$$\vec{R}(\xi,\zeta) = \frac{\Delta z}{N_x N_y f\alpha} \boldsymbol{S}(\xi,\zeta)\boldsymbol{H}(\xi,\zeta)\boldsymbol{E}\vec{C}(\xi,\zeta) \tag{11}$$

where $\boldsymbol{S}(\xi,\zeta)$ is a diagonal matrix with elements $S_{m,m}(\xi,\zeta) = \mathrm{sinc}(\Delta z(\xi\cos(\phi_m)+\zeta\sin(\phi_m)))$, $H_{m,n}(\xi,\zeta) = e^{-2\pi i(\xi\cos(\phi_m)+\zeta\sin(\phi_m))n\Delta z}$, and $\boldsymbol{E}$ is a diagonal matrix with elements $E_{n,n} = \eta(\lambda_n)$.

To this point we have neglected the effects of noise. If we assume that the noise is additive, then Eq. 11 becomes

$$\vec{R}(\xi,\zeta) = \frac{\Delta z}{N_x N_y f\alpha} \boldsymbol{S}(\xi,\zeta)\boldsymbol{H}(\xi,\zeta)\boldsymbol{E}\vec{C}(\xi,\zeta) + \vec{N}(\xi,\zeta), \tag{12}$$

where $\vec{N}(\xi,\zeta)$ is the 2D discrete spatial Fourier transform of the noise vector.

At the core of the proposed spectral imaging technique are the matrix inversions required to calculate $\vec{C}(\xi,\zeta)$ from $\vec{R}(\xi,\zeta)$. Though most of the matrices are well behaved, many are singular. The method for dealing with the singular matrices is discussed in the following section, but we can make some useful observations by inspection of Eq. 12. The matrix $\boldsymbol{S}(\xi,\zeta)$ will be singular when $\Delta z(\xi\cos(\phi_m)+\zeta\sin(\phi_m)) = 1.0$. By selecting Δz to be much less than the largest value of $1.0/(\xi\cos(\phi_m)+\zeta\sin(\phi_m))$, we can prevent $\boldsymbol{S}(\xi,\zeta)$ from becoming singular. Selecting a small value for Δz increases the computational demands of the inversion, but does not adversely affect it otherwise. If we assume square pixels, the largest value of $\xi\cos(\phi_m)+\zeta\sin(\phi_m)$ will be $1/\sqrt{2}\Delta x$. So Δz must be less than $\sqrt{2}\Delta x$.

5. INVERSION OF THE MATRICES IN THE PRESENCE OF NOISE

In order to solve Eq. 12 for $\vec{C}(\xi,\zeta)$ we need to invert each of the matrices in Eq. 12. Both $\boldsymbol{S}(\xi,\zeta)$ and $\boldsymbol{E}$ are easily inverted, but $\boldsymbol{H}(\xi,\zeta)$ is potentially singular. Since the matrix $\boldsymbol{H}(\xi,\zeta)$ may be singular, we utilize the singular value decomposition (SVD) of a matrix[6]. SVD factors an MxN matrix into a product of an MxN column-orthogonal matrix $\boldsymbol{U}$, an NxN diagonal matrix $\boldsymbol{W}$ with real non-negative elements, and an NxN orthogonal matrix $\boldsymbol{V}$ or in tableau form:

$$\begin{bmatrix} \\ \boldsymbol{H} \\ \\ \end{bmatrix} = \begin{bmatrix} \\ \boldsymbol{U} \\ \\ \end{bmatrix} \begin{bmatrix} w_{11} & & \\ & \ddots & \\ & & w_{nn} \end{bmatrix} \begin{bmatrix} \\ \boldsymbol{V} \\ \\ \end{bmatrix}. \tag{13}$$

Since $\boldsymbol{U}$ and $\boldsymbol{V}$ are column orthonormal, we find

$$\begin{bmatrix} \\ \boldsymbol{U}^\dagger \\ \\ \end{bmatrix} \begin{bmatrix} \\ \boldsymbol{U} \\ \\ \end{bmatrix} = \begin{bmatrix} \\ \boldsymbol{V}^\dagger \\ \\ \end{bmatrix} \begin{bmatrix} \\ \boldsymbol{V} \\ \\ \end{bmatrix} = \begin{bmatrix} \\ \mathbf{1} \\ \\ \end{bmatrix}, \tag{14}$$

where the dagger indicates Hermitian adjoint (transpose conjugate). The inverse of the diagonal matrix $\boldsymbol{W}$ is illustrated by

$$\begin{bmatrix} 1/w_{11} & & \\ & \ddots & \\ & & 1/w_{nn} \end{bmatrix} \begin{bmatrix} w_{11} & & \\ & \ddots & \\ & & w_{nn} \end{bmatrix} = \begin{bmatrix} & \mathbf{1} & \end{bmatrix}. \tag{15}$$

We find that for an MxN matrix $\boldsymbol{H}$ we can make a pseudo-inverse $\boldsymbol{V}^{\dagger}\boldsymbol{W}^{-1}\boldsymbol{U}^{\dagger}$, such that

$$\mathbf{1} = \boldsymbol{V}^{\dagger}\boldsymbol{W}^{-1}\boldsymbol{U}^{\dagger}\boldsymbol{H}. \tag{16}$$

We estimate $\vec{C}(\xi,\zeta)$ by $\tilde{C}(\xi,\zeta)$ where

$$\tilde{C}(\xi,\zeta) = \frac{N_x N_y f\alpha}{\Delta z}\boldsymbol{E}^{-1}\boldsymbol{V}^{\dagger}(\xi,\zeta)\boldsymbol{W}^{-1}(\xi,\zeta)\boldsymbol{U}^{\dagger}(\xi,\zeta)\boldsymbol{S}^{-1}(\xi,\zeta)\vec{R}(\xi,\zeta), \tag{17}$$

where we have taken care to ensure that the diagonal elements of $\boldsymbol{E}$ and $\boldsymbol{S}(\xi,\zeta)$ are non-zero, so that corresponding inverses are well defined. Only the matrix $\boldsymbol{W}(\xi,\zeta)$ is potentially singular.

In the context of the SVD decomposition, a singular matrix is one in which one or more of the w_{ii} is zero. Mathematicians speak of ill-conditioned matrices as those where one of the w_{ii} is within a computer's floating point accuracy of zero. In this application the noise in the recorded image data $r(x,y,\phi_m)$ is effectively divided by $w_{ii}(\xi,\zeta)$, so if the value of any of the $w_{ii}(\xi,\zeta)$ is small, the noise will be greatly amplified. If we consider the matrix at a single spatial frequency, when the value of $w_{ii}(\xi,\zeta)$ is less than one the noise will be amplified relative to the signal. To circumvent this problem we replace $\boldsymbol{W}^{-1}(\xi,\zeta)$ with $\tilde{\boldsymbol{W}}^{-1}(\xi,\zeta)$, where $1/w_{ii}(\xi,\zeta)$ is replaced by $w_{ii}(\xi,\zeta)/(w_{ii}^2(\xi,\zeta)+\epsilon^2)$, where ϵ has a value of approximately one. The issue of selecting the correct value of ϵ is complicated by the fact that we invert a matrix at each spatial frequency, and we wish to optimize the aggregate spectral imager performance. From experience we have found that the optimal value of ϵ is approximately 1.5.

Figure 2 is a graphical representation of the values of $w_{ii}(\xi,\zeta)$ illustrating where in the frequency domain information is lost for the current AMSI configuration. The dark regions in Fig. 2 are analogous to the missing cone in limited angle computed tomography [7]. While the physical interpretation is identical to that in [7], the mathematical treatment here differs from that commonly found in the literature since this treatment uses a hybrid of Fourier and SVD determined basis functions.

As Fig. 2 indicates, all of the spectral information is lost at zero spatial frequency. A physical understanding of this phenomena can by obtained by considering the sequence of frames recorded by the AMSI for a monochromatic source of infinite extent that is perfectly uniform. Since the source is uniform and of infinite extent, the sequence of frames will be unaffected by the rotation of the prism (if we consider a system with no field stop). The same sequence of recorded frames would be recorded for any wavelength monochromatic source or for any broad-band extended source that was perfectly uniform. Therefore there is no way to algorithmically distinguish the spectral content of a spatially uniform source, and the zero spatial frequency information is lost. It is possible that the effect of a field stop on this analysis could be used to reduce the amount of lost information, but this type of analysis is a method of utilizing prior knowledge and we have deferred it to future work.

In general, when one of the $w_{ii}(\xi,\zeta)$ values becomes too small, there is insufficient information to determine how the measured signal should be distributed among the spectral bands. The pseudo-inverse assumes a "smooth" distribution of the signal among the spectral bands (i.e. the distribution with minimum norm [6]). In practice the effect of the "smoothing" is that when $w_{ii}(\xi,\zeta)$ is approximately equal to ϵ at a given spatial frequency, the resulting spectral reconstruction is affected by an increase in the noise and an increase in the spectral cross-talk at that spatial frequency. When $w_{ii}(\xi,\zeta)$ is much less than ϵ the resulting reconstruction is predominantly affected by an increased spectral cross-talk. We have found that the fidelity of the measurement and the signal to noise ratio at 1/2 Nyquist is quite good, while the fidelity at the high and low spatial frequencies can be poor. These effects will be discussed in greater detail in the experimental results section; however, at this point we can conclude that it is unlikely that

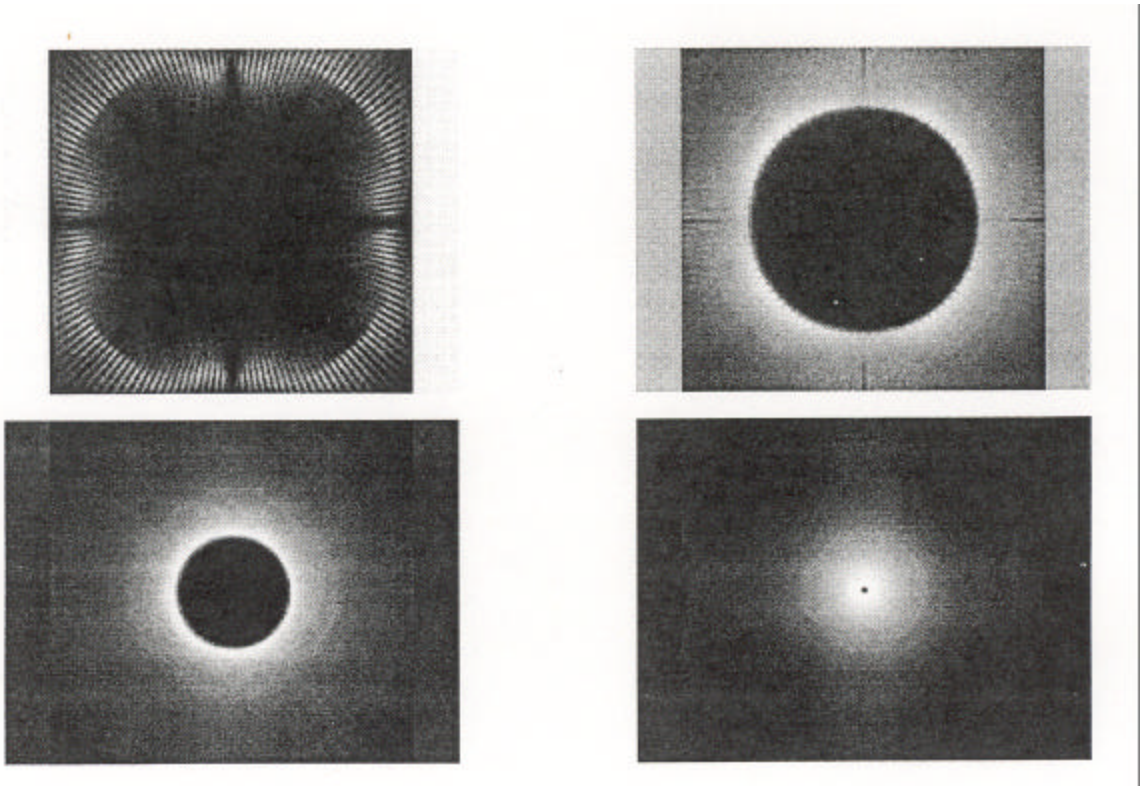

Figure 2: Illustration of the $w_{ii}(\xi,\zeta)$ values as a function of spatial frequency. Zero spatial frequency is in the center of each image. Bright and dark regions correspond to large and small values of $w_{ii}(\xi,\zeta)$ respectively. The sequence from left to right, top to bottom corresponds to descending spectral frequency data. The lower right image corresponds to image features that change slowly as a function of wavelength (low spectral frequencies). The upper left image corresponds to image features that change rapidly as a function of wavelength (high spectral frequencies). The dark region in the center of each image corresponds to the spatial/spectral frequencies where information has been lost.

the AMSI will in and of itself find application as an imaging spectral radiometer; however, future work will address optical and computational methods for restoring the lost information.

Though Fig. 2 represents the condition of only one AMSI configuration, it illustrates features that are generally true for these exotic spectral imagers [1, 2, 3, 4, 8]. The low-spatial frequency matrices tend to be ill-conditioned, while the zero spatial frequency matrix is singular. The poor conditioning of the low spatial frequency matrices is due to the limited separation of the chromatic images. Since we are unable to record infinite dispersion image (that which corresponds to the top looking down onto the λ axis), the lowest spatial frequency matrices will remain ill-conditioned.

6. ALTERNATIVE DISPERSER CONFIGURATIONS

Throughout this discussion the dispersing element has been assumed to be a direct vision prism. Although the functional form of $\boldsymbol{H}(\xi,\zeta)$ is dependent on the dispersing element configuration, the general solution discussed in Eqs. 1-5 is not. This section will summarize other potential disperser configurations. Each of these configurations is aimed at reducing the size of the region of ill-conditioned matrices.

The field stop can be used to reduce, or eliminate, the ill-conditioned region. In the limit of imaging the field stop onto a pixel, the ill-conditioned region is eliminated. Multiple point field stops could be used to obtain a radiometrically correct spectral imagery; however, with this approach the effective efficiency is dramatically reduced. More exotic field stop masks could be used to maintain high efficiency while minimizing the ill-conditioned region. In the limit of reducing the field stop to a slit, the AMSI becomes a conventional scanned slit spectrometer.

A variable pitch grating (for example a surface acoustic wave disperser) has the advantage that, unlike the direct vision prism, the dispersion is variable. This variability could be a very powerful tool in controlling the region of ill-conditioned matrices, but keeping the image on the focal plane while the grating pitch was changing would be a challenge. The variable pitch grating approach is also limited by the performance and availability of variable pitch gratings.

Another method for achieving variable dispersion is to combine two direct vision prisms[9]. When the two prism are co-aligned, the dispersion is effectively doubled; when they are anti-aligned, the dispersion is effectively nulled. The variable dispersion prism adds the freedom to control the dispersion over a limited range, but considerably complicates the prism alignment problems.

A third method of obtaining variable dispersion is to combine a dispersive element with a zoom lens[10]. This technique is intended to reduce the region of ill-conditioned matrices and can be combined with any of the disperser techniques. A Variant of this approach is to use an anamorphic lens with a short focal length in the dispersion direction and a long focal length in the cross dispersion direction. The goal here is to eliminate the region of ill-conditioned matrices by imaging the field stop onto a pixel in the dispersion direction (similar to the approach discussed in [11]). In practice one finds that it is difficult to vary the optical power enough to execute these approaches for systems with even modest fields of view.

A lens intentionally designed to have a large amount of longitudinal chromatic aberration can also be used as a dispersive element [12]. In this implementation, the focal plane array is longitudinally displaced with respect to the image plane, and an image is recorded for each of a variety of image displacements. This approach is similar to three dimensional microscopy techniques. Although this approach keeps the light on the focal plane, it does not facilitate in the recovery of the low-spatial frequency image information, and only passes high-spatial frequency information for the in-focus spectral band. In terms of AMSI performance, this is an inefficient approach.

A grating can be combined with any inversion prism to create a dispersive element. Dove, Reversion, or Pechan prisms will all provide the inversion needed. In this case, it is the grating that produces the dispersion, while the prism provides a simple way to rotate the direction of dispersion while keeping the light on the focal plane (the grating remains fixed while the prism is rotated). This configuration has the advantage of linear dispersion, and the

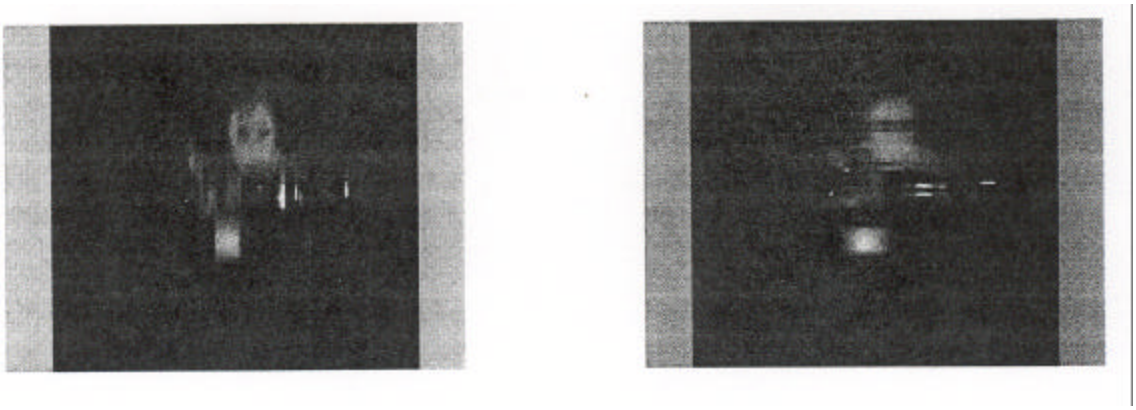

Figure 3: Examples of the imagery as recorded by the infrared camera with the direct vision prism at two different orientations.

disadvantages of the direct vision prism. It is also more difficult to achieve a large clear aperture with this approach.

A series of prisms of varying dispersion sequentially placed in the optical path is the spectral imaging approach described in [1]. This approach is conceptually very similar to medical imaging techniques, but it has low efficiency due to the time required to swap dispersive elements.

The final approach is a series of crossed transmission gratings that remain fixed combined with a field stop that limits the image size to be much smaller than the focal plane array [2, 3, 4]. In this approach, the sequence of images $r_a(x, y)$ are all recorded simultaneously on different portions of the focal plane array. The field stop is used to keep the images from overlapping, and the stack of gratings is used to obtain multiple combinational dispersions (each order transmitted through the first grating is diffracted into multiple orders on the second grating). The advantage of this approach is that enough data is recorded in each frame to construct a 3-D image. The disadvantages are that the field of view is limited, and that the number of spectral bands one can obtain are limited.

7. EXPERIMENTAL RESULTS

To demonstrate the performance of the AMSI we imaged a laboratory scene that contained several different types of objects in order to evaluate performance over as wide a range of conditions as is possible. The scene contained a monochromatic slit source (the exit slit of a monochromator), a broad-band point source, several broad-band extended sources at different temperatures, and the visage of a co-worker.

Examples of the imagery as recorded by the infrared camera are shown in Fig. 3. The two frames in Fig. 3 are part of the 80 frame sequence used to construct the spectral image. The frames were gathered by continuously rotating the prism so that one complete revolution was completed in 80 frames. Since the camera used to collect the data operated at 30 frames/sec, the data acquisition took 2.67 sec.

Fig. 3 illustrates the impact of the prism and its orientation on the recorded images. One sees that in the direction of dispersion, the image appears blurred: the visibility of the vertical bars in the four bar pattern and that of the horizontal wires just below the face is strongly affected by the prism orientation, bright point sources become line segments the orientation of which indicate the angular orientation of the prism. The streak of the dispersed point source at the right of Fig. 3 shows the effect of the atmospheric absorption band at 4.3μm.

The extraction of the spectral data from the input sequence was performed on a Sun workstation. In order to speed up the inversion process, the matrix inverses were stored on hard disk as short integers (16 bits). The size of the inverse matrices was just over 600 Mbytes. The fact that the precision of the inverse was only 16 bits did not appear to adversely affect the results. The runtime of the inversion was approximately 7 minutes.

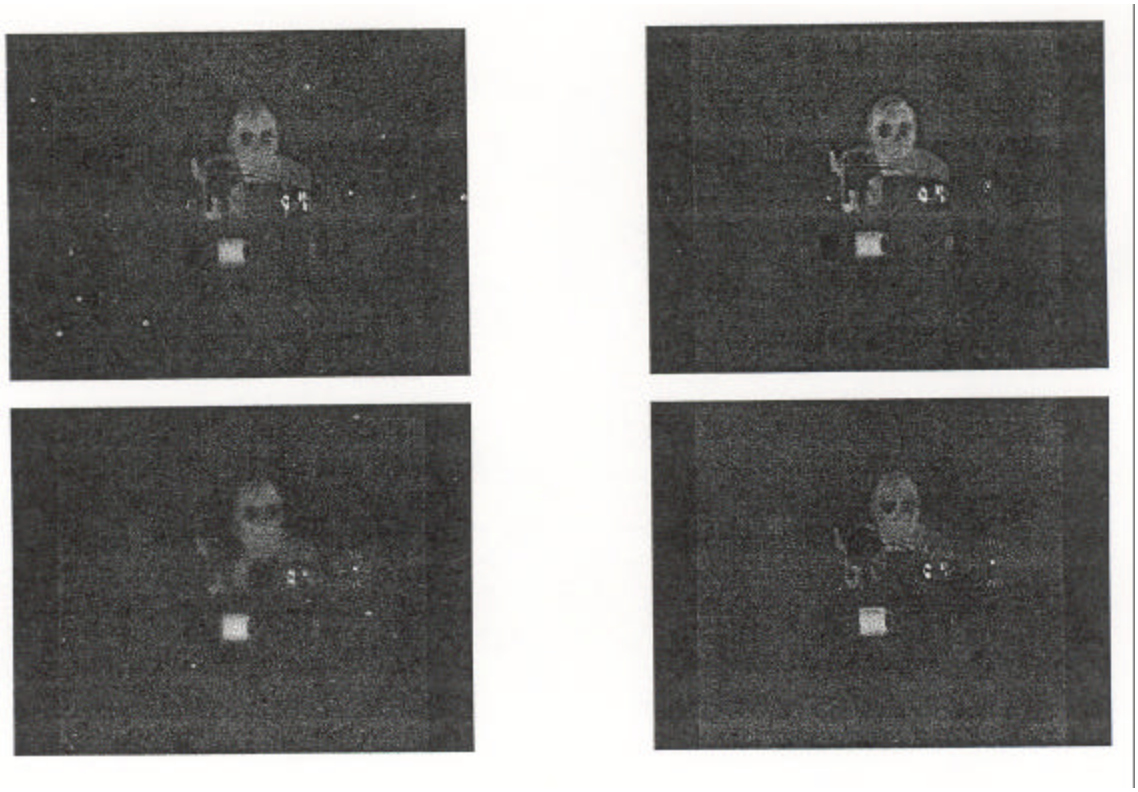

Figure 4: A sample of the narrow band spectral images obtained from the data set featured in Fig. 3. The center wavelength of each image is, 3.61 μm (upper left), 3.87 μm (upper right), 4.33 μm (lower left), and 4.49 μm (lower right).

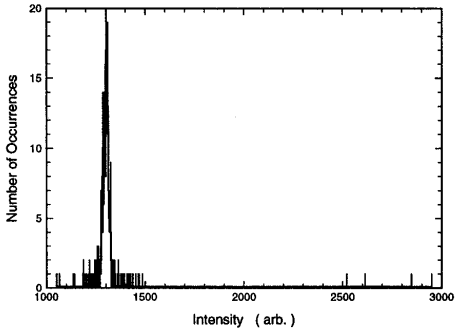

Figure 5: Histogram of the region surrounding the bright point source in the 3.87 μm image of Fig. 4. The four bright pixels (levels 2500-3000) are the source itself. The artifacts (levels 1400-1500) are much closer to the background ($\approx$ 1300) than suggested by Fig. 4.

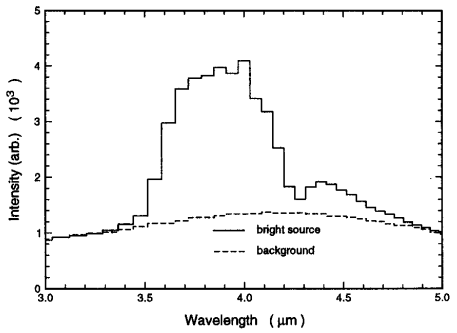

Figure 6: Spectral profile of a bright source compared to that of the background illustrating the atmospheric absorption at 4.3 μm.

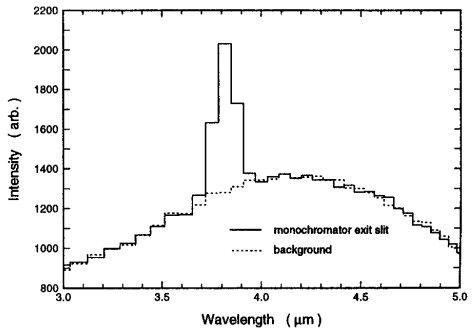

Figure 7: Spectral profile of the monochromator exit slit.

Four slices of the three-dimensional spectral image are shown in Fig. 4. Examination of Fig. 4 reveals both the strong points and the current problems with this spectral imaging technique. We begin by addressing the dominant problem, the artifact surrounding bright point sources. The artifact results from the finite angular resolution of the sampling grid (80 prism orientations), which is also observable in Fig. 2. The amplitude of the artifact is greatly exaggerated in Fig. 4 since a nonlinear image mapping technique was used to represent both the bright sources and the background features in the same image[13]. A more representative evaluation of the magnitude of the artifact is shown in Fig. 5, where the magnitude of the artifact is shown relative to the magnitude of the bright source. From Fig. 5 we estimate that the artifacts are approximately an order of magnitude less intense than the source.

A comparison of the four-bar pattern in various spectral bands Fig. 4 reveals the effect of the atmospheric absorption band at 4.3 μm on scene modulation. The effect of the atmosphere is also observed as a dip in the spectral profile of a bright source as shown in Fig. 6. In this case the atmospheric absorption can be used to verify the spectral calibration of the AMSI.

To quantify the spectral resolution of the AMSI, we analyze the spectral profile of the monochromator exit slit shown in Fig. 7. From Fig. 7 we estimate the full-width-at-half-max resolution to be about 1/10 μm. Although the

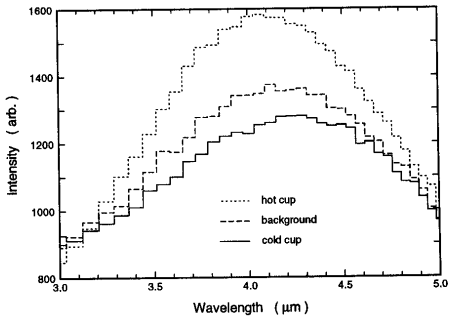

Figure 8: Spectral profiles of a hot cup, the background and a cold cup.

measured spectral resolution may be somewhat broader than the actual resolution due to the finite bandwidth of the monochromator, this value is consistent with an estimate based only on the prism dispersion, optical focal length, optical blur diameter, and the pixel size.

Figure 8 illustrates the effect of source temperature on the spectral profile. To a large extent the spectral profiles are determined by the product of the blackbody radiation function and the Schottky response function. Each of the three sources obeys the general trend of maximum intensity signal at approximately 4 μm with diminishing signal at the short wavelengths due to the decreasing blackbody emission and diminishing signal at the long wavelengths due to the decreasing Schottky response. Also apparent in Fig. 8 is the characteristic of hotter sources to emit more radiation at all wavelengths with the peak shifted to shorter wavelengths.

8. CONCLUSIONS

We have demonstrated that spectral imaging can be accomplished using the AMSI approach. Even though this approach has only been demonstrated in the mid-infrared, it is generally applicable to any spectral band where 2-dimensional imaging arrays and direct vision prisms are available. For the price of a direct vision prism, any staring camera can be converted to a spectral imager.

We have also shown that some of the scene information is lost by the AMSI. In particular, the low-spatial frequency / high-spectral frequency information is missing from the resulting spectral imagery which leads to limited degradation of the image quality. However; since the AMSI images all of the spectral bands on all of the pixels all of the time the treatment of the high spatial frequency information is very efficient.

Systems that require multi-band spectral imagery over large fields of view, but do not require radiometric information are most likely to benefit from this approach.

9. ACKNOWLEDGMENTS

The author thanks Bill Ewing and Steve DiSalvo for fabricating the infrared camera; John Mead for fabricating the data acquisition interface; Virgil Vickers for software support; Linda Bouthillette for graphical assistance; and Jerry Silverman, Paul Pellegrini and Freeman Shepherd for critical reading of this manuscript. This work was supported by AFOSR Task 2305J1 under Horst Wittmann and Gerry Witt.

10. REFERENCES

[1] F. V. Bulygin, G. N. Vishnyakov, G. G. Levin, and D. V. Karpukhin, "Spectrotomography-a new method of obtaining spectrograms of 2-d objects", *Opt. Spectrosc. (USSR)*, 71, pp. 561-563, December (1991).

[2] M. R. Descour, "Nonscanning no-moving-parts imaging spectrometer", Published in this proceeding.

[3] T. Okamoto and I. Yamaguchi, "Simultaneous acquisition of spectral image information", *Optics Letters*, 16, pp. 1277-1279, August (1991).

[4] T. Okamoto, A. Takahashi, and I. Yamaguchi, "Simultaneous acquisition of spectral and spatial intensity distribution", *Applied Spectroscopy*, 47, pp. 1198-1202, August (1993).

[5] J. M. Mooney, "Spectral imaging via computed tomography", *Proc. 1994 Meeting of the IRIS specialty group on passive sensors*, 1, pp. 203-215, March (1994).

[6] W. H. Press, B. P. Flannery, S. A. Teukolsky, and W. T. Vetterling, *Numerical Recipes in C*, pages 60 - 72. Cambridge University Press, New York, 1988.

[7] H. H. Barrett, "Editorial: Limited-angle tomography for the nineties", *The Journal of Nuclear Medicine*, 31, pp. 1688-1692, October (1990).

[8] M. Hinnrichs and M. A. Massie, "Image multispectral sensing: a new and innovative instrument for hyperspectral imaging using dispersive techniques", Published in this proceeding.

[9] S. Wein, private communication.

[10] P. A. Bernhardt and J. A. Antoniades, "Hyperspectral imaging with rotational spectrotomography", Published in this proceeding.

[11] T. Cook, "Ultraviolet imaging spectroscopy of dust in the interstellar medium", Published in this proceeding.

[12] D. G. Mooney, private communication.

[13] J. Silverman, J. M. Mooney, and V. E. Vickers, "Display of wide dynamic range infrared images from ptsi schottky barrier cameras", *Optical Engineering*, 29, pp. 97-104, February (1990).